

Active hyperspectral imaging for vegetation based on a supercontinuum laser and SPAD array

Wang Xin-Ru¹, Li Chun-Tao^{1,2*}, Jiang Chang-Hui¹, Yue Jiang³, Su Zi-Kang¹, Wu Xiang⁴, Hu Pei-Lun⁵,
Chen Yu-Wei⁶, Liu Di⁷

- (1. College of Automation Engineering, Nanjing University of Aeronautics and Astronautics, Nanjing 211106, China;
2. National Center of Technology Innovation for Advanced Aviation Equipment, Chengdu 610074, China;
3. College of Mechanics and Engineering Science, Hohai University, Nanjing 211100, China;
4. School of Automation, Nanjing University of Science and Technology, Nanjing 210094, China;
5. Department of Forest Sciences, University of Helsinki, Helsinki 00014, Finland;
6. Hangzhou Institute for Advanced Study, Hangzhou 310024, China;
7. School of Automation, Nanjing Institute of Technology, Nanjing 211167, China)

Abstract: Hyperspectral LiDAR (HSL) is an emerging active sensing technique that can simultaneously acquire spectral and spatial information for quantitative remote sensing applications. However, most existing HSL systems acquire spectral and spatial information point by point, which limits the acquisition of image-like hyperspectral data and dense 3D point clouds. In this paper, the authors presented a hyperspectral imaging LiDAR system based on a chip-scale single-photon avalanche diode (SPAD) array (768×576) and a supercontinuum laser source (SPAD-HSL). A focus-tunable emitting system was designed to provide broadband illumination, while a SPAD-array-based receiving system was developed to enable wavelength-selective detection using optical filters. Based on the proposed SPAD-HSL system, hyperspectral measurements were conducted on a total of 12 leaf samples, including 5 species and various physiological states, under different detection distances and angles. The acquired spectral data were subsequently compared with spectrometer measurements, demonstrating that the proposed system enables active hyperspectral imaging acquisition and achieves high spectral consistency.

Key words: Active hyperspectral imaging, Hyperspectral LiDAR, SPAD Array

PACS:

Introduction

Hyperspectral LiDAR (HSL) has become one of the prominent research directions in active remote sensing recently. By integrating the three-dimensional spatial sensing capability of conventional LiDAR with the fine spectral discrimination capability, The HSL enables the simultaneous acquisition of target spatial structure and spectral characteristics^[1]. This capability provides significant potential for applications in ecological and environmental monitoring, ocean and inland water observation and resource exploration^[2-4]. Conventional LiDAR systems typically employ a single wavelength or a limited number of discrete laser wavelengths to retrieve target range and

backscattered intensity, enabling high-precision and high-resolution three-dimensional measurements. However, the inherently limited spectral dimensionality significantly constrains their capability for material discrimination. In contrast, hyperspectral remote sensing acquires rich spectral information across continuous wavelength bands. However, these systems are predominantly based on passive imaging, which limits spatial resolution and hampers the retrieval of vertical structural information.

Multispectral laser scanning (MLS) has been explored for vegetation remote sensing applications by combining multiple monochromatic laser sources at discrete wavelengths, enabling simultaneous multi-wavelength measurements under identical illumination geometry^[5-7]. However, extending spectral coverage and resolution by

Received date: 2026-XX-XX,

收稿日期: 2026-

Foundation items: Supported by the National Natural Science Foundation of China (62573232, 62503224 61903190); the Natural Science Foundation of Jiangsu Province (BK20241388).

Biography: WANG Xin-Ru(2001-), female, Huangshan Anhui, Ph. D. candidate. Research area involves autonomous positioning of unmanned aerial vehicles and laser detection technology. E-mail: xr_wang@nuaa.edu.cn.

* **Corresponding author:** E-mail: lct13770925493@163.com;

increasing the number of laser sources is impractical due to elevated system complexity, cost, power consumption, and limited scalability. As a result, most MLS systems operate at previously selected wavelengths tailored to specific applications, providing only sparse spectral information and failing to capture continuous spectral profiles comparable to spectrometers, which restricts their versatility in precision agriculture and vegetation biochemical analysis.

To address these limitations, hyperspectral LiDAR (HSL) systems based on supercontinuum (SC) laser sources have been developed, offering ultra-broadband emitting and enabling dense spectral sampling through appropriate filtering and detection architectures^[8-10]. Starting from the first demonstration of SC-based HSL, subsequent advances have progressively increased spectral channel numbers, extended spectral coverage from the visible to the shortwave infrared, and improved spectral resolution via tunable filtering techniques, i. e., LCTFs and AOTFs, thereby enabling the concurrent acquisition of 3D structural and hyperspectral profiles for vegetation and material characterization^[11-14].

However, restricted by the APD detectors, current HSLs have the following shortcomings:

(1) Constrained by the manufacturing technology of the APD detectors, most existing HSL systems are built with a single-point APD detector to detect the reflected laser echoes. As a result, only one point cloud and one spectral band information can be acquired at a time. It is time-consuming to collect tens of bands spectral information with millions of point clouds. Part of the HSL systems incorporate a simple two-dimensional scanning mechanism to perform limited spatial scanning and obtain point clouds over a certain area^[15]; however, the performance of such systems is still constrained by the limitations of the scanning mechanism.

(2) Existing HSL systems generally require the construction of range and incidence-angle correction models. Since the laser return intensity depends on range, incidence angle, and surface material properties, corrections for range and incidence angle are necessary. This requirement limits the further application and broader deployment of HSL systems.

With the development of SPAD manufacturing technology, large-scale imaging APD array chips have become possible and its cost decreases a lot^[16-17]. In this paper, a SPAD with a resolution of 768×576 is employed in the SPAD-HSL to replace the single APD to set up a LiDAR with the hyperspectral imaging function. This paper presents a hyperspectral imaging LiDAR system based on a large-scale SPAD array. The main innovative contributions are summarized as follows.

(1) For the first time, active spectral data acquisition with an imaging resolution of 512×384 (after cropping) is achieved using a large-scale SPAD array. The proposed system adopts a supercontinuum laser as the laser source, a focus-tunable laser emitting subsystem is installed followed by. The backscattered echo intensity is detected by the SAPD array, enabling active hyperspec-

tral imaging, in which a filter is employed at the receiving system to perform the received spectral bands selection. Compared with conventional single-point-scanning multispectral LiDAR systems, the proposed approach achieves spectrometer-like hyperspectral imaging while simultaneously acquiring the point clouds in a manner analogous to MEMS-LiDAR systems.

(2) Assessment experiments of the proposed SPAD-HSL has been conducted and analyzed. For the first time, multispectral imaging for vegetation was carried out. Spectral imaging profiles are compared with that from the hyperspectral spectrometer, the correlation of the spectral profiles from the SPAD-HSL and hyperspectral spectrometer is analyzed and presented.

1 System design

The SPAD-HSL system was designed based on the schematic illustration in Fig. 1. A supercontinuum laser is employed as the laser source, which is triggered by the computer. The emitting parameters of the supercontinuum laser are configured via dedicated computer control software, which allows for adjustment of the output energy percentage to precisely control the emitted optical power, thereby accommodating different detection ranges and target reflectance characteristics. In the laser emitting system, the laser beam is first collimated by a fiber collimator to form a high-quality parallel beam. Next, the collimated laser enters a variable-magnification projection lens, which projects the beam onto the target surface. In the optical receiving system, the reflected signal from the targets first passes through a set of interchangeable optical filters and is then collected by the receiving lens, which focuses the filtered light onto the SPAD array to enable spatial imaging and spectral information acquisition of the targets.

1.1 Laser emitting system

In the SPAD-HSL system, a SC-5 supercontinuum laser (Anyang Laser, Wuhan, China) is employed as the laser source, providing a spectral wavelength range of 450~2400 nm and a repetition rate of 5 MHz, with a total output power exceeding 1w. In this study, the laser power was set to 100% according to the manufacturer's specifications to ensure stable operation. After collimation, the supercontinuum laser enters a projection lens, which is designed as a variable magnification projection lens. The projection lens is a customized optical module comprising four lens groups with a 0.5 mm entrance aperture, as illustrated in Fig. 2. The lens adopts a manual focus adjustment mechanism, in which the focal state is varied by moving a variable lens group to control the laser spot size. Given its custom configuration, the lens performance is characterized by its illumination angle variation capability. Specifically, the minimum illumination angle is $0.3^\circ \pm 0.02^\circ$, while the maximum illumination range reaches $50^\circ \pm 2^\circ$. In addition, the zooming time from the narrow-angle state to the wide-angle state is less than 12 s, allowing the system to flexibly adapt to targets at different distances while maintaining stable illumination and imaging performance.

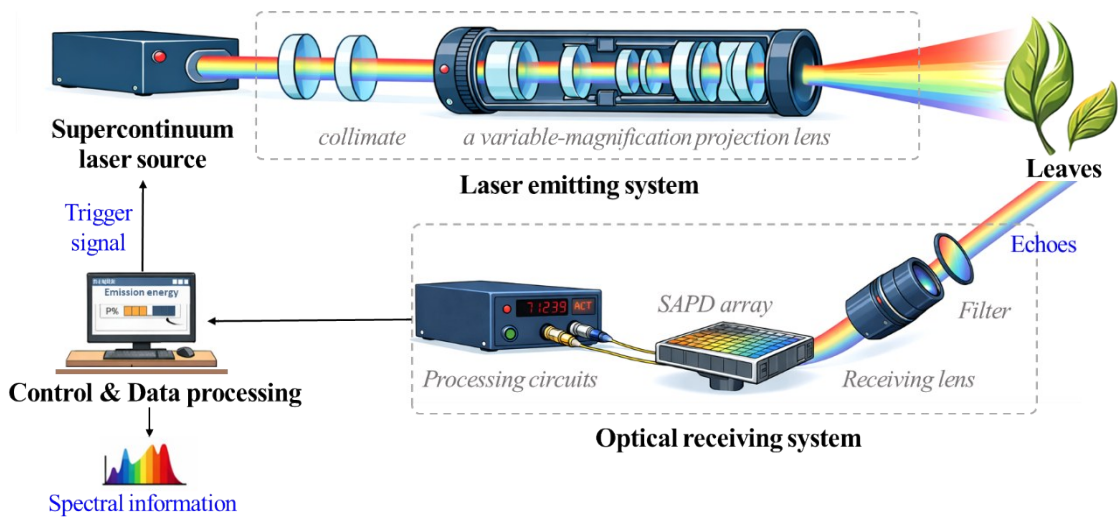


Fig. 1 Schematic of a SPAD-HSL system
图 1 SPAD-HSL 系统框架图

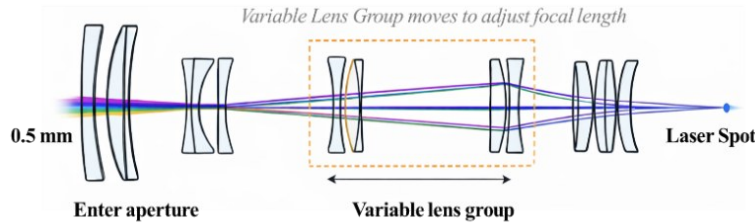


Fig. 2 Schematic of the Lens Wide Angle
图 2 广角镜头示意图

1.2 Optical receiving system

The optical receiving system was designed based on the schematic illustration in Fig. 3, consisting of optical filters, a receiving lens, a SPAD array (Fig. 4), and processing circuits. For wavelength-selective detection, a set of interchangeable optical filters (Hengyang Optical, HNIF series) with dimensions of $\varnothing 25.4 \times 6$ mm, a full-width at half-maximum (FWHM) of 10 nm, and a transmittance greater than 90% is mounted in front of the receiving lens, covering the spectral range from 580 nm to 750 nm, with a resolution of 10 nm. To facilitate filter switching, a stepper motor is used to rotate the filter wheel, automatically switching filters upon button press. Following the optical filters, a 16mm fixed-focus lens is employed to capture the reflected laser signals and positioned at the front of the SPAD array. To meet the requirements for signal reception, the lens features a relatively short focal length and a wide field of view exceeding 23° , enabling effective measurement of the reflected laser signals over a broad range. According to the manufacturer's datasheet, under room temperature conditions, the employed SPAD array exhibits a photon detection efficiency (PDE) of $\geq 10\%$, ensuring sufficient sensitivity for weak reflected signal detection. The readout circuitry and driving module of the SPAD array are implemented based on a System on Chip (SOC) architecture using an ARM7 pro-

cessor, with a Linux-based system running on the SOC to write to the APD registers, enabling the APD to operate in ranging mode.

Although certain constraints such as budget limitations have influenced the system's current configuration, the current system configuration has successfully met the requirements for imaging functionality validation of the proposed SPAD-HSL system. At this stage, manual intervention is still required for switching filters, and the system operates sequentially to capture each wavelength band. To enable real-time multi-waveband detection and faster switching, an Acousto-Optic Tunable Filter (AOTF) is currently being incorporated in the next research phase.

2 Data Processing

2.1 Image normalization

To eliminate the influence of laboratory illumination conditions on the grayscale response of the images, a local white background region was randomly selected as an intensity reference to perform relative normalization on the original color images. First, the original color images were converted into grayscale images according to a standard weighted formula:

$$I_{\text{gray}} = 0.299 * R + 0.587 * G + 0.114 * B, \quad (1)$$

A $s_1 \times s_1$ pixel region was then randomly selected from the white background, where s_1 is the size of the

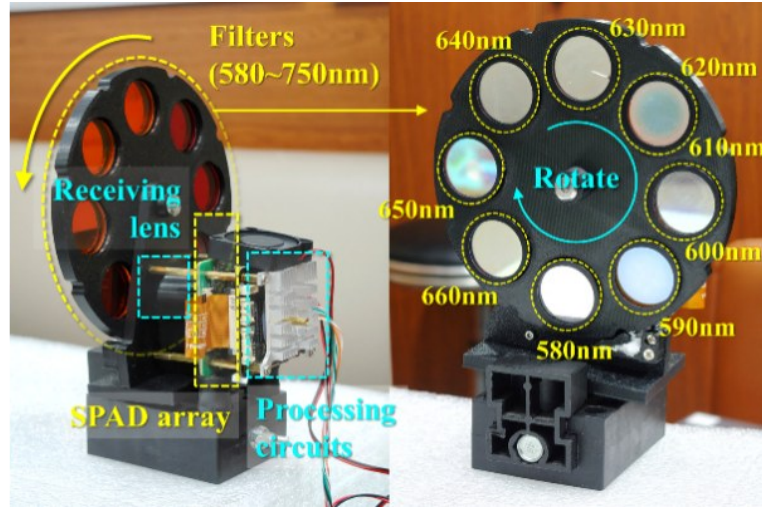


Fig. 3 Optical receiving system hardware prototype
图3 光接收系统硬件原型

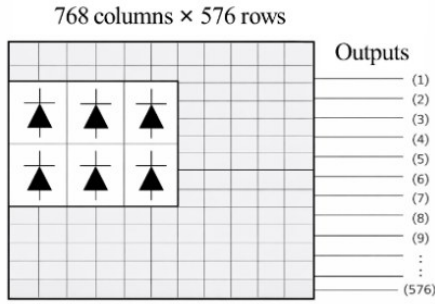


Fig. 4 Schematic of the SPAD array
图4 SPAD阵列示意图

white pixel region. Then the mean grayscale value of this region μ_{white} was calculated as the reference for the corresponding image frame.

$$\mu_{white} = \frac{1}{s_1^2} \sum_{i=1}^{s_1^2} I_{gray}(x_i, y_i), \quad (2)$$

Then, the grayscale value of each pixel in the entire image was divided by this reference value, thereby completing the white-reference-based relative normalization of the image.

$$I_{norm}(x, y) = \frac{I_{gray}(x, y)}{\mu_{white}}. \quad (3)$$

2.2 HSL Backscattered Echo Intensity Extraction

A fixed $s_2 \times s_2$ pixel region of the leaves was randomly selected across the 18 normalized images acquired over the wavelength range of 580~750 nm, where s_2 is the size of the pixel region. The mean grayscale value of this region was then calculated at each wavelength, yielding the relative backscattered echo intensity response sequence of the sampling pixel regions \bar{I}_n^{HSL} in the visible wavelength range.

$$\bar{I}_n^{HSL} = \frac{1}{s_2^2} \sum_{(x,y) \in \Omega_n} I_{norm}^{(n)}(x, y), n = 1, 2, \dots, 18, \quad (4)$$

where $I_{norm}^{(n)}$ represents the n -th normalized image, and Ω_n

represents the sets of pixels in the sampling pixel region, defined as $\Omega_n = \{(x, y) | x_0 \leq x < x_0 + s_2, y_0 < y_0 + s_2\}$.

2.3 Correlation Analysis

Under identical laser illumination conditions, a reference spectrometer was employed to measure the echo intensities of the sampling pixel regions. The acquired spectrometer spectrum was resampled by linear interpolation to obtain echo intensities from 580 to 750 nm with a 10 nm spectral resolution. Similarly, the interpolated intensities were normalized using the same procedure described in Step A, yielding the normalized spectral intensities of spectrometer, denoted as \bar{I}_n^{SPM} . Finally, a correlation analysis was conducted between the backscattered echo intensities measured by the proposed SPAD-HSL system and the spectral intensities measured by the spectrometer for the same pixel regions, validating the spectral accuracy and reliability of the proposed SPAD-HSL system. The correlation coefficient was calculated defined as:

$$R_n = \frac{\sum_n \bar{I}_n^{HSL} \bar{I}_n^{SPM}}{\sqrt{\sum_n \bar{I}_n^{HSL^2} \sum_n \bar{I}_n^{SPM^2}}}, n = 1, 2, \dots, 18. \quad (5)$$

3 Experiments

Based on the schematic described in Section 1 and methodology described in Section 2, the SPAD-HSL system hardware prototype (Fig. 5) was set up in the laboratory for system performance evaluation. The laboratory experiments were conducted to assess the spectral consistency between the proposed SPAD-HSL system and a reference spectrometer, to validate its hyperspectral imaging capability. The experiment selected five groups of leaf samples, including Ligustrum, Osmanthus, Camphor, Photinia, and Gardenia. Each group contains leaves with different physiological states, resulting in a total of 12 leaf samples (Fig. 6). These samples were used to provide diverse spectral responses for system performance validation. The experiments were conducted in

two stages. In the first stage, the first and second groups of leaf samples were measured at a detection distance of 0.8 m under two detection angles, 90° and 60° . A total of two datasets were obtained in this stage, which aimed to evaluate the effectiveness of the system under different physiological states and leaf species. Considering that sample leaves are prone to rapid dehydration and physiological changes, which may affect their spectral characteristics, an additional three groups of leaf samples were introduced in the second stage. Experiments were conducted at two detection distances, 0.8 m and 1.6 m, and under two detection angles, 90° and 60° . In this stage, a total of 12 experimental datasets were collected to further verify the system performance under varying detection distances and angles.

3.1 Imaging Effect

Hyperspectral imaging experiments were conducted in the 580~750 nm wavelength range based on a large-scale SPAD array. Compared with single-point scanning approaches^[18], the SPAD array enables simultaneous acquisition of spectral information at multiple spatial loca-

tions, allowing for rapid and active imaging. The SPAD array itself has a physical resolution of 768×576 , however, due to limitations in the processing power, the acquired images are cropped and reduced to a final resolution of 512×384 pixels. This adjustment ensures an optimal balance between the array's physical resolution and the practical processing constraints of the system.

As shown in Fig. 6, a fixed white pixel region with a size of $s_1 = 20$ was selected for image normalization, as described in Section 2.1, and pixel values were sampled at consistent spatial locations for subsequent spectral correlation analysis. For the leaf samples, the sampling region size s_2 was determined according to the detection distance. Specifically, under the 0.8 m detection condition, the sampling region size was set to $s_2 = 10$. However, under the 1.6 m detection condition, the leaf occupied a smaller pixel area in the captured images due to the increased imaging distance. To reduce the influence of excessive exposure pixels and background interference, the sampling region size was correspondingly reduced to $s_2 = 2$, thereby improving the reliability and

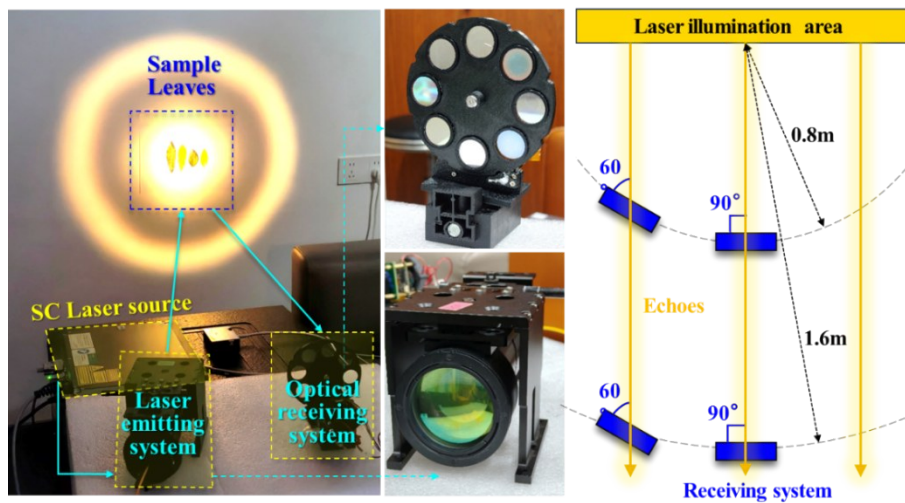


Fig. 5 SPAD-HSL system hardware prototype
图5 SPAD-HSL系统硬件原型

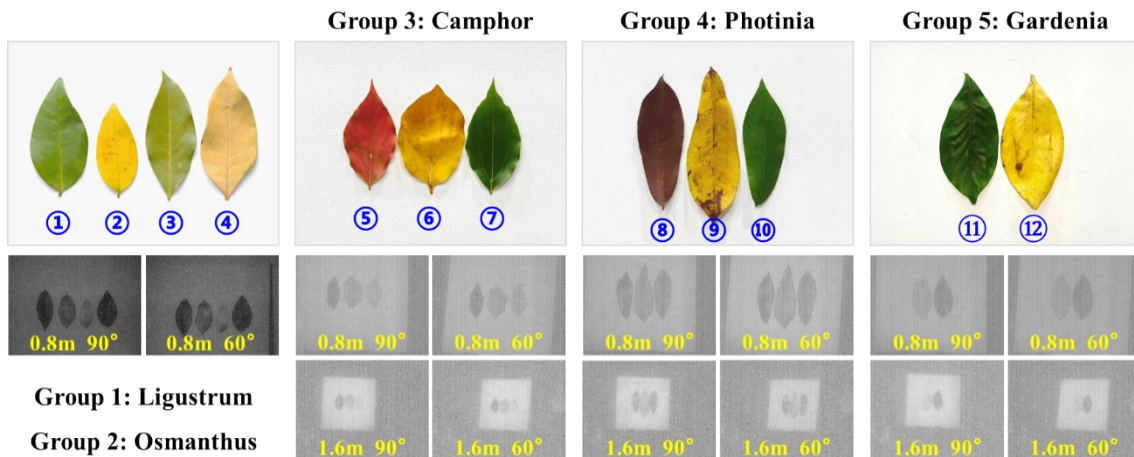


Fig. 6 Leaf sample and their imaging effects
图6 树叶样本及其成像效果

consistency of the spectral analysis results.

3.2 Correlation Analysis

Table 1 presents the correlation coefficients between the laser echo intensities extracted from selected pixel regions of 12 leaf samples and the corresponding measurements obtained using the spectrometer under varying experimental conditions, including two distances (0.8 m and 1.6 m) and two incident angles (60° and 90°). Figure 8 illustrates the mean correlation coefficients and their standard deviations for twelve leaf samples across all experimental conditions. Notably, samples #1, #5, and #12 exhibit relatively larger standard deviations, which can be attributed to the random selection of pixel regions for analysis and the non-uniform surface characteristics of the leaves. Overall, the correlation coefficients remain very high across all leaf types, detection distances and angles, indicating that the proposed SPAD-HSL system provides robust and generally highly consistent spectral measurements.

In the first stage of the experiments, the effectiveness of the SPAD-HSL system was evaluated across different physiological states and leaf species based on leaf

samples from Group 1 (*Ligustrum*) and Group 2 (*Osmanthus*). As shown in Table 1 and Fig. 9, in the comparison between yellow and green leaves, yellow leaf samples exhibit significantly higher correlation than the green leaf samples. This difference is mainly attributed to the degradation of chlorophyll and the increase in other pigments, such as carotenoids, which results in smoother spectral reflectance changes in yellow leaves. Particularly in the visible to near-infrared regions, the spatial spectral heterogeneity in yellow leaves is reduced, enhancing measurement consistency. In the comparison between leaf species, *Ligustrum* leaves show slightly higher correlation than *Osmanthus* leaves, which may be related to the surface structure and venation pattern of the leaves. *Ligustrum* leaves typically have a smoother and more uniform surface, leading to more consistent light reflection. In contrast, *Osmanthus* leaves have more prominent venation, which causes uneven light reflection and scattering, increasing measurement discrepancies.

In the second stage of the experiments, additional experiments were conducted to evaluate the performance of the proposed SPAD-HSL system under different detec-

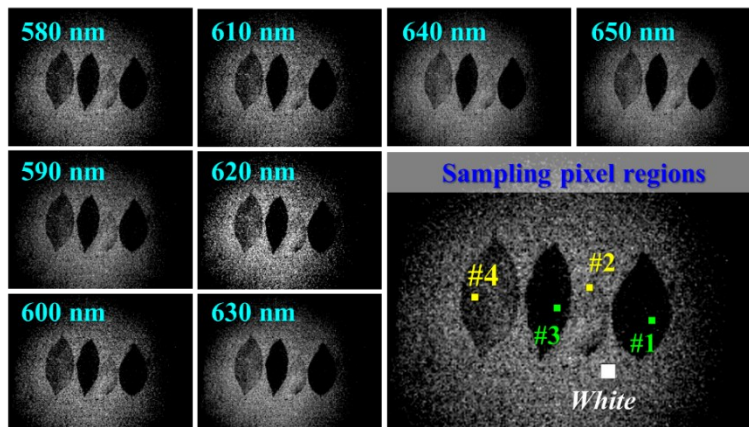


Fig. 7 Normalized images and sampling pixel regions
图7 归一化图像和采样像素区域

Table 1 Correlation coefficients of leaf samples under different experimental conditions
表 1 不同实验条件下的叶片样本相关系数

Number	Group	Leaf sample	Correlation coefficients			
			0.8m, 90°	0.8m, 60°	1.6m, 90°	1.6m, 60°
#1	Ligustrum	green leaf	0.9453	0.8852	/	/
#2		yellow leaf	0.9977	0.9962	/	/
#3	Osmanthus	green leaf	0.9406	0.9408	/	/
#4		yellow leaf	0.9852	0.987	/	/
#5	Camphor	red leaf	0.9682	0.9329	0.9725	0.9823
#6		yellow leaf	0.9585	0.9533	0.9768	0.9911
#7		green leaf	0.9340	0.9645	0.9658	0.9795
#8	Photinia	red leaf	0.9722	0.9562	0.9801	0.9631
#9		yellow leaf	0.9878	0.9521	0.9877	0.9912
#10		green leaf	0.9637	0.9422	0.9374	0.9702
#11	Gardenia	green leaf	0.9562	0.9506	0.9652	0.9629
#12		yellow leaf	0.9565	0.9517	0.9931	0.9964

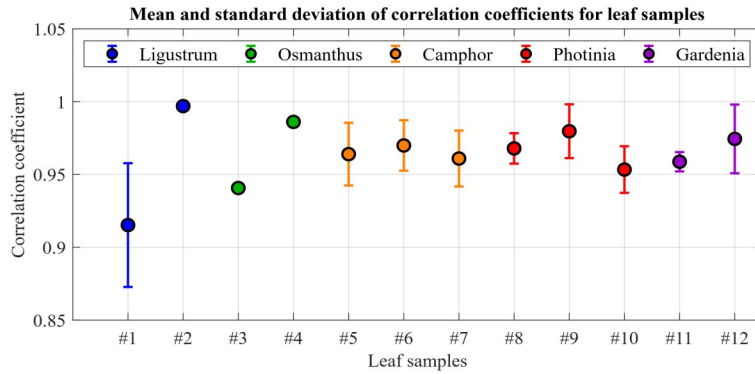


Fig. 8 Mean and standard deviation of correlation coefficients for leaf samples
图 8 叶片相关系数的平均值与标准差

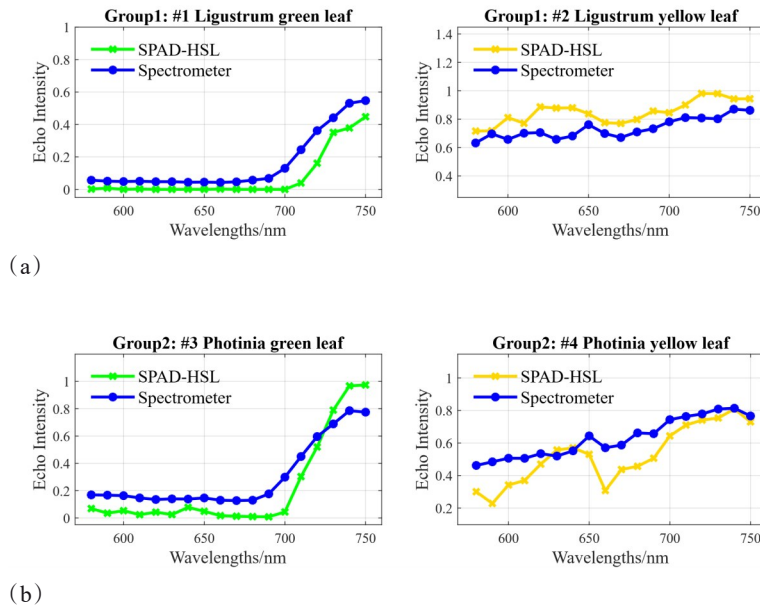


Fig. 9 Echo intensity comparison for different leaf samples at fixed distance and angle (a) Groups 1 Ligustrum; (b) Groups 2 Osmanthus
图 9 不同叶片样本在固定距离与角度下的回波强度比较 (a) 第 1 组 女贞树叶; (b) 第 2 组 桂树叶

tion distances and angles, using leaf samples from Group 3 (Camphor), Group 4 (Photinia) and Group 5 (Gardenia). As shown in Table 1, the echo intensities measured at different distances and angles are highly consistent across all leaf samples, with most samples exhibiting correlation coefficients above 0.95, demonstrating the robust measurement reproducibility. Fig. 10 illustrates the echo intensity spectra of Photinia leaves (samples #8, #9, and #10) under each distance-angle combination. In this dataset, some curves exhibit noticeable fluctuations, which can be attributed to several factors inherent to the SPAD-HSL system. The high sensitivity of the SPAD array enables the detection of weak optical signals but also makes the measurements more susceptible to noise, resulting in deviations in the echo intensity curves. This effect is further amplified at shorter detection distances, where the stronger received signal and larger effective sampling regions increase the possibility of capturing heterogeneous leaf structures and

background variations, thereby enhancing spectral fluctuations. Despite these localized instabilities, the overall spectral trends remain consistent, and high correlation with spectrometer measurements is maintained across distances and angles, demonstrating the stable hyperspectral imaging capability of the SPAD-HSL system under varying experimental conditions.

3.3 Discussion

Although the similarity between the spectral profiles obtained from the proposed SPAD-HSL system and the spectrometer is evident, certain differences remain, which can be attributed to the following reasons.

1) The SPAD-array-based imaging system acquires data from multiple pixel regions simultaneously, resulting in weak signal intensities for each pixel, while the optical filter bandwidth further limits signal strength, increasing the influence of noise on the measurement results. We believe that using optical filters with narrower bandwidths can effectively mitigate noise and improve im-

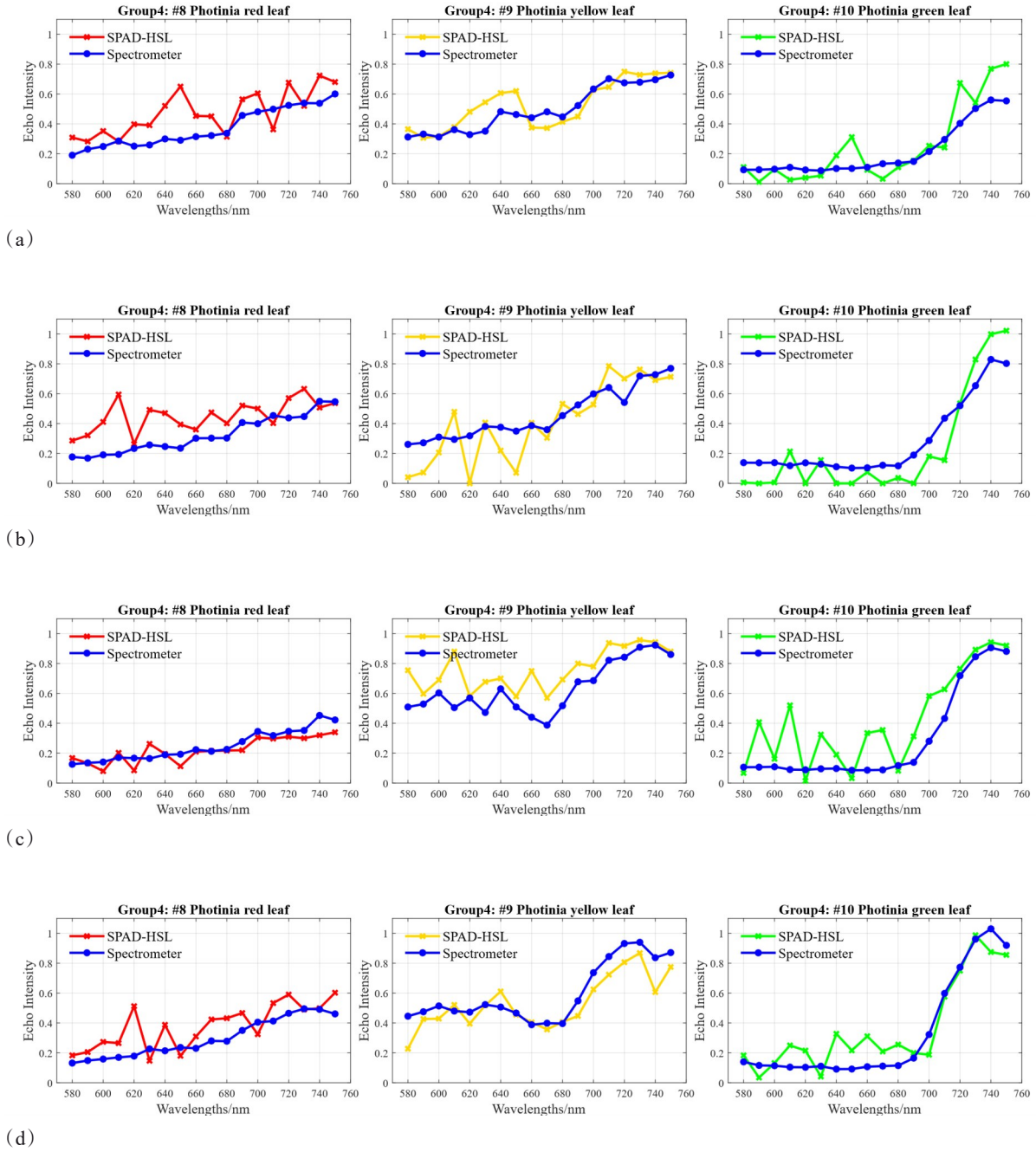


Fig. 10 Echo intensity comparison of the same leaf sample at different distances and angles (Group 4 Photinia) (a) detection distance = 0.8m, detection angle = 90° ; (b) detection distance = 0.8m, detection angle = 60° ; (c) detection distance = 1.6m, detection angle = 90° ; (d) detection distance = 1.6m, detection angle = 60°

图 10 同一样本叶片在不同距离与角度下的回波强度比较(第 4 组 石楠树叶)(a) 探测距离 = 0.8m, 探测角度 = 90° ; (b) 探测距离 = 0.8m, 探测角度 = 60° ; (c) 探测距离 = 1.6m, 探测角度 = 90° ; (d) 探测距离 = 1.6m, 探测角度 = 60° ;

aging performance.

2) The SPAD array is highly sensitive and capable of detecting extremely weak signals; however, this high sensitivity also increases its susceptibility to noise, leading to measurement deviations and instability.

3) The supercontinuum laser source may exhibit an uneven energy distribution across different wavelengths, which affects the signal strength at various bands and

consequently impacts the spectral response of the entire measurement system. In this study, the analysis focuses on relative spectral variations, for accurate quantitative measurements, further calibration of the source spectrum or system response should be incorporated in future work.

4) Although this study focuses on active hyperspectral acquisition, the SPAD array used is already widely deployed in automotive LiDAR. Combined with pulse

time-of-flight (TOF) principles, it also has the potential to generate 3D point clouds. Timing synchronization and data readout are still under development, and future work will aim to complete point cloud acquisition and explore the capabilities of “spectral + spatial” joint sensing for vegetation analysis and environmental modeling.

4 Conclusions

In this paper, a SPAD-HSL system is firstly proposed and a hardware prototype is demonstrated in the laboratory. Unlike conventional single-point scanning multispectral LiDAR systems, the proposed system utilizes active supercontinuum laser illumination and the parallel, high-speed detection capability of the SPAD array to enable active hyperspectral imaging and rapid data acquisition, and is insensitive to detection angle variations. Twelve leaf samples, covering five plant species and various physiological states, were measured by the SPAD-HSL system under laboratory conditions at multiple detection distances and angles to evaluate spectral consistency. Experimental results validate the accuracy and reliability of the proposed system for active hyperspectral imaging, marking a significant advancement in LiDAR technology by transitioning from single-band to multi-band imaging. This capability supports the further development of active remote sensing technologies.

References

- [1] Kuras A, Brell M, Rizzi J, et al. Hyperspectral and lidar data applied to the urban land cover machine learning and neural-network-based classification: A review [J]. *Remote sensing*, 2021, 13(17): 3393.
- [2] Zhang Hui-Jing, Chen Lin-Sheng, Wu Hao-Hao, et al. Hyperspectral LiDAR for Subsea Exploration: System Design and Performance Evaluation[J]. *Electronics*, 2025, 14(8): 1539.
- [3] Shao Hui, Chen Yu-Wei, Yang Zhi-Rong, et al. Feasibility study on hyperspectral LiDAR for ancient Huizhou-style architecture preservation[J]. *Remote Sensing*, 2019, 12(1): 88.
- [4] Sun Hai-Bin, Wang Zhen, Chen Yu-Wei, et al. Preliminary verification of hyperspectral LiDAR covering VIS-NIR-SWIR used for objects classification [J]. *European Journal of Remote Sensing*, 2022, 55(1): 291-303.
- [5] Hakula A, Ruoppa L, Lehtomäki M, et al. Individual tree segmentation and species classification using high-density close-range multispectral laser scanning data[J]. *ISPRS Open Journal of Photogrammetry and Remote Sensing*, 2023, 9: 100039
- [6] Zheng Ke-Xin, Yang Shui-Qing, Che Hao, et al. Multispectral three-dimensional Scheimpflug LiDAR for plant monitoring: system design and experimental validation [J]. *Optics and Lasers in Engineering*, 2026, 201: 109731.
- [7] Yang Ning, Li Shi-Fa, Chen Si, et al. Development of a Black Carbon Aerosol Sensor Based on Multispectral Laser Scattering [J]. *IEEE Sensors Journal*, 2026. DOI: 10.1109/JSEN.2026.3667931.
- [8] Jia Jian-Xin, Jiang Chang-Hui, Li Wei, et al. Hyperspectral LiDAR-based plant spectral profiles acquisition: performance assessment and results analysis [J]. *Remote Sensing*, 2021, 13(13): 2521.
- [9] Li Wei, Jiang Chang-Hui, Chen Yu-Wei, et al. A liquid crystal tunable filter-based hyperspectral LiDAR system and its application on vegetation red edge detection [J]. *IEEE geoscience and remote sensing letters*, 2018, 16(2): 291-295.
- [10] Shao Hui, Zhang Hu-Long, Hu Pei-Lun, et al. Feasibility study of forest wood-boring pest detection base on hyperspectral LiDAR [J]. *International Journal of Remote Sensing*, 2024, 45(6): 1926-1948.
- [11] Jiang Chang-Hui, Chen Yu-Wei, Wu Hao-Hao, et al. Study of a high spectral resolution hyperspectral LiDAR in vegetation red edge parameters extraction [J]. *Remote Sensing*, 2019, 11(17): 2007.
- [12] Xu Lu, Shi Shuo, Gong Wei, et al. Mapping 3D plant chlorophyll distribution from hyperspectral LiDAR by a leaf-canopy radiative transfer model [J]. *International Journal of Applied Earth Observation and Geoinformation*, 2024, 127: 103649.
- [13] Chen Yu-Wei, Li Wei, Juha Hyypä, et al. A 10-nm spectral resolution hyperspectral LiDAR system based on an acousto-optic tunable filter [J]. *Sensors*, 2019, 19(7): 1620.
- [14] Hu Pei-Lun, Chen Yu-Wei, Imangholiloo M, et al. Urban tree species classification based on multispectral airborne LiDAR [J]. *红外与毫米波学报*, 2025, 44(2).
- [15] Wang Qi-Yu, Li Qi-Wei, Cao Yang, et al. Time-stretch multispectral LiDAR enabled by a supercontinuum laser and a single-point detector [J]. *Optics Express*, 2025, 33(18): 39068-39080.
- [16] Tan Chang-Sheng, Kong Wei, Huang Geng-Hua, et al. Long-range daytime 3D imaging lidar with short acquisition time based on 64×64 Gm-APD array [J]. *IEEE Photonics Journal*, 2022, 14(3): 1-7.
- [17] Ulku A C, Bruschini C, Antolović I M, et al. A 512×512 SPAD image sensor with integrated gating for widefield FLIM [J]. *IEEE Journal of Selected Topics in Quantum Electronics*, 2018, 25(1): 1-12.
- [18] Shao Hui, Cao Zheng, Li Wei, et al. Feasibility study of wood-leaf separation based on hyperspectral LiDAR Technology in indoor circumstances [J]. *IEEE Journal of Selected Topics in Applied Earth Observations and Remote Sensing*, 2021, 15: 729-738.

基于超连续光源与 SPAD 阵列的植被主动高光谱成像

汪馨茹¹, 李春涛^{1,2*}, 蒋长辉¹, 岳江³, 苏子康¹, 吴祥⁴, 胡佩纶⁵, 陈育伟⁶,
刘娣⁷

(1. 南京航空航天大学自动化学院, 南京 211106;

2. 国家高端航空装备技术创新中心, 成都 610074;

3. 河海大学力学与工程科学学院, 南京 211100;

4. 南京理工大学自动化学院, 南京 210094;

5. 赫尔辛基大学 森林科学系, 赫尔辛基 00014 芬兰;
6. 国科大杭州高等研究院, 杭州 310024;
7. 南京工程学院 自动化学院, 南京 211167)

摘要: 高光谱激光雷达是一种新兴的主动传感技术, 可同时获取光谱和空间信息, 用于定量遥感应用。然而, 现有大多数 HSL 系统采用逐点采集方式, 这限制了类图像高光谱数据和高密度三维点云的获取。本文提出了一种基于芯片级单光子雪崩二极管阵列 (768×576) 和超连续光源的高光谱成像激光雷达系统 (SPAD-HSL)。该系统设计了可调焦发射结构以实现宽带照明, 并构建了基于 SPAD 阵列的接收系统, 通过光学滤波器实现波长选择性探测。基于所提 SPAD-HSL 系统, 对共计 12 片叶片样本 (包括 5 种不同植物及多种生理状态) 在不同探测距离和角度下进行了高光谱测量。随后, 将获得的光谱数据与光谱仪测量结果进行了对比, 结果表明, 该系统能够主动获取高光谱图像, 并实现较高的光谱一致性。

关键词: 主动高光谱成像; 高光谱激光雷达; SPAD 阵列

中图分类号: S771.8

文献标识码: A